



HAL
open science

Bars and boxy/peanut bulges in thin and thick discs

Fragkoudi Francesca, Paola Di Matteo, Misha Haywood, Gómez Anita,
Françoise Combes, David Katz, Benoit Semelin

► To cite this version:

Fragkoudi Francesca, Paola Di Matteo, Misha Haywood, Gómez Anita, Françoise Combes, et al.. Bars and boxy/peanut bulges in thin and thick discs: I. Morphology and line-of-sight velocities of a fiducial model. *Astronomy and Astrophysics - A&A*, 2017, 606, pp.A47. 10.1051/0004-6361/201630244 . hal-02191447

HAL Id: hal-02191447

<https://hal.science/hal-02191447>

Submitted on 16 Jan 2021

HAL is a multi-disciplinary open access archive for the deposit and dissemination of scientific research documents, whether they are published or not. The documents may come from teaching and research institutions in France or abroad, or from public or private research centers.

L'archive ouverte pluridisciplinaire **HAL**, est destinée au dépôt et à la diffusion de documents scientifiques de niveau recherche, publiés ou non, émanant des établissements d'enseignement et de recherche français ou étrangers, des laboratoires publics ou privés.

Bars and boxy/peanut bulges in thin and thick discs

I. Morphology and line-of-sight velocities of a fiducial model

F. Fragkoudi¹, P. Di Matteo¹, M. Haywood¹, A. Gómez¹, F. Combes^{2,3}, D. Katz¹, and B. Semelin²

¹ GEPI, Observatoire de Paris, PSL Research University, CNRS, Univ. Paris Diderot, Sorbonne Paris Cité, Place Jules Janssen, 92195 Meudon, France

e-mail: francesca.fragkoudi@obspm.fr

² Observatoire de Paris, LERMA, CNRS, PSL Univ., UPMC, Sorbonne Univ., 75014 Paris, France

³ Collège de France, 11 place Marcelin Berthelot, 75005 Paris, France

Received 14 December 2016 / Accepted 29 May 2017

ABSTRACT

We explore trends in the morphology and line-of-sight (los) velocity of stellar populations in the inner regions of disc galaxies using N -body simulations with a thin (kinematically cold) and a thick (kinematically hot) disc which form a bar and a boxy/peanut (b/p) bulge. The bar in the thin disc component is $\sim 50\%$ stronger than the thick disc bar and is more elongated, with an axis ratio almost half that of the thick disc bar. The thin disc b/p bulge has a pronounced X-shape, while the thick disc b/p is weaker with a rather boxy shape. This leads to the signature of the b/p bulge in the thick disc being weaker and further away from the plane than in the thin disc. Regarding the kinematics, we find that the los velocity of thick disc stars in the outer parts of the b/p bulge can be higher than that of thin disc stars, by up to 40% and 20% for side-on and Milky Way-like orientations of the bar, respectively. This is due to the different orbits followed by thin and thick disc stars in the bar-b/p region, which are affected by two factors. First, thin disc stars are trapped more efficiently in the bar-b/p instability and thus lose more angular momentum than their thick disc counterparts and second, thick disc stars have large radial excursions and therefore stars from large radii with high angular momenta can be found in the bar region. We also find that the difference between the los velocities of the thin and thick disc in the b/p bulge (Δv_{los}) correlates with the initial difference between the radial velocity dispersions of the two discs ($\Delta\sigma$). We therefore conclude that stars in the bar-b/p bulge will have considerably different morphologies and kinematics depending on the kinematic properties of the disc population they originate from.

Key words. methods: numerical – galaxies: kinematics and dynamics – galaxies: structure – galaxies: spiral – galaxies: bulges

1. Introduction

Bars are ubiquitous features in the local Universe, with about two thirds of disc galaxies containing bars with variable strengths (Eskridge et al. 2000; Menéndez-Delmestre et al. 2007; Barazza et al. 2008; Aguerri et al. 2009; Gadotti 2009). Boxy/peanut/X-shaped (b/p) bulges (also referred to as boxy/peanuts, or b/p's) are structures which extend out of the plane of nearly half of all edge-on disc galaxies in the local Universe (Lütticke et al. 2000). Numerical simulations and orbital structure analysis have shown the intimate link between bars and b/p's, by demonstrating that once a bar forms, a b/p will likely form soon after (e.g. Combes et al. 1990; Martínez-Valpuesta et al. 2006) since b/p's are caused by vertical orbital instabilities which cause the bar to puff out vertically from the plane of the disc (e.g. Binney 1981; Pfenniger & Friedli 1991; Skokos et al. 2002; Portail et al. 2015). Recent work has also shown how b/p's can affect the evolution of disc galaxies, by reducing the bar-driven gas inflow (Fragkoudi et al. 2015, 2016; for reviews on these topics the reader is referred to Athanassoula 2016, and references therein).

Furthermore, from extensive photometric and spectroscopic studies of the Milky Way bulge, we now know that the inner region of the Milky Way contains a bar and a b/p (Weiland et al. 1994; Dwek et al. 1995; Howard et al. 2009; Nataf et al. 2010; McWilliam & Zoccali 2010; Ness & Lang 2016). Indeed, recent

results suggest that the main component of the Milky Way bulge is a b/p (Ness et al. 2012, 2013; Wegg & Gerhard 2013); estimates place an upper limit on the mass of a possible classical bulge between ~ 2 –10% (Shen et al. 2010; Kunder et al. 2012, 2016; Di Matteo et al. 2014; Debattista et al. 2017).

Owing to the ubiquitous nature of thick discs in observed (Burstein 1979; Tsikoudi 1979; Yoachim & Dalcanton 2006) and simulated galaxies (Abadi et al. 2003; Bird et al. 2013; Stinson et al. 2013; Martig et al. 2014), along with the various formation scenarios proposed for them (Quinn et al. 1993; Brook et al. 2004; Schönrich & Binney 2009; Qu et al. 2011; Martig et al. 2014; Minchev et al. 2015; Haywood et al. 2015), the question of the interplay between such a population and structures such as bars and b/p's naturally arises. In the Milky Way in particular, due to the small scalelength of the α -enhanced thick disc population (Bensby et al. 2011; Bovy et al. 2012), it follows that the chemically defined thick disc is centrally concentrated; this, along with recent results from chemical evolution models which indicate that the mass of the thick disc could be of the same order as that of the thin disc (Haywood et al. 2013; Snaith et al. 2015), point to the fact that the thick disc will have an important contribution in terms of mass in the central region of the Milky Way. There have also been recent claims that (geometrically defined) thick discs make up a significant fraction of the baryonic content of galaxies (Comerón et al. 2011). Therefore, the question of how thick discs are mapped into a bar and

a b/p bulge is of foremost interest to our understanding of the structure and evolution of disc galaxies in general, and to the Milky Way in particular.

In this study we therefore explore how thin and thick discs are mapped into a bar and a b/p bulge. This work is further motivated by the fact that, with the exception of few recent studies, not much work has been done on the composite nature of bars and b/p bulges in galaxies with both a thin and a thick disc, whether these are modelled as discrete components or with a continuum of populations (see e.g. Bekki & Tsujimoto 2011a,b; Di Matteo 2016, for models with discrete stellar populations; and e.g. Debattista et al. 2017; Athanassoula et al. 2017 for models with a continuum of stellar populations). It is important to note that when employing models with discrete stellar populations, as in the case of the models presented here, we do not necessarily imply that galaxies are made up of two distinct components (for example, studies of stellar populations in the Milky Way have shown that it has a disc whose properties vary continuously with scaleheight; see Bovy et al. 2012). Modelling galaxies with discrete components essentially helps to simplify the problem, while also allowing for controlled simulations (in which the scalelengths, scaleheights, and kinematic properties can be varied at will), and lends itself to understanding the trends that will be followed by stellar populations with different kinematic properties.

While we know that stars in the disc will get trapped in the bar instability as a function of how kinematically hot the population is (as was found by studies of individual discs, e.g. Hohl 1971; Athanassoula 1983; Athanassoula & Sellwood 1986; Combes et al. 1990; Athanassoula 2003), there has not been a systematic study on how the properties of bars and b/p bulges vary as a function of the properties of the kinematically hot/thick disc component, such as its mass and scalelength. We will therefore address the dynamics, morphology, and kinematics of bars and b/p bulges in simulations with both thin and thick discs, of various masses and scalelengths in a series of papers (Fragkoudi et al., in prep.) in order to understand how bars map stellar populations with different dynamical properties into the inner regions of galaxies. In this paper – the first in the series – we explore a fiducial simulation, focusing on the main trends in morphology and line-of-sight velocities of stars in bars and b/p’s in set-ups with both thin and thick discs. We focus on giving physical interpretations for these observed trends, based largely on the exchange of angular momentum which the two populations are subject to.

The structure of the paper is as follows. In Sect. 2 we describe the simulations and the initial conditions. In Sect. 3 we discuss the basic morphological features of our fiducial model with both a thin and a thick disc, and we show how these discs are mapped into the bar and b/p bulge. In Sect. 4 we focus on the kinematics, specifically on the line-of-sight (los) velocity of the models, and show that the los of the thick disc can be higher than that of the thin disc in the b/p region. In Sect. 5 we explore how the angular momentum redistribution and the radial velocity dispersion affect the morphology and the los velocities of the thin and thick disc stars in the bar-b/p. In Sect. 6 we discuss observational studies relevant to these results, and in Sect. 7 we summarise the main conclusions of the paper.

2. Simulations and initial conditions

In this study we use an N -body simulation which has both a thin and a thick disc, with characteristic scaleheights of 0.3 and 0.9 kpc, respectively, to study disc galaxies with stellar

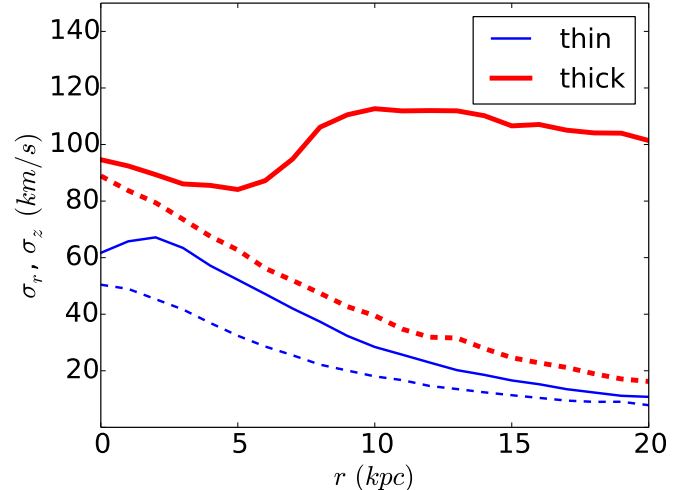


Fig. 1. Radial (solid) and vertical (dashed) velocity dispersion profiles of the thin (blue) and thick (red) discs in the initial conditions of the fiducial model used in this study.

populations with different kinematic properties. The model is a simplification of reality since it is unlikely that most disc galaxies contain two very well-separated and distinct components, as is evidenced by studies of stellar populations in the Milky Way which have shown that it has a disc whose properties vary continuously with scaleheight (e.g. Bovy et al. 2012). This discretisation reduces the complexity of the model, and can be used to understand the trends that will be followed by the stellar populations in the Milky Way and external disc galaxies.

The initial conditions of the discs explored in this study are obtained using the algorithm of Rodionov et al. (2009), the so-called “iterative method”. The algorithm constructs equilibrium phase models for stellar systems, using a constrained evolution so that the equilibrium solution has a number of desired parameters. As we do not have tight constraints on the radial and tangential velocity dispersion of galaxies in the local Universe (and even less so at higher redshifts) we do not impose a profile to these velocity dispersions, instead allowing the system to converge to an equilibrium solution. The only constraining parameter is the density distribution of the two discs, which are described by a Miyamoto-Nagai profile (Binney & Tremaine 2008) with a characteristic radius r_D of 4.7 kpc; the velocity dispersion is let to evolve unconstrained, with the requirement that the initial conditions (ICs) generated are in equilibrium. At the end of the iterative method we obtain velocity dispersion profiles for the thin and thick discs as shown in Fig. 1, which are correspondingly kinematically cold and hot, also in terms of the radial velocity dispersion. We note that the vertical velocity dispersion profile naturally converges to that expected from the equation

$$\sigma_z(r) = \sqrt{c\pi G\Sigma(r)h_z}, \quad (1)$$

which is derived from the Poisson and Jeans equations, and which relates the vertical distribution of stars (h_z) and their vertical velocity dispersion (σ_z) to the mass distribution (Σ) as a function of radius r (where the constant c depends on the form of the height function; see van der Kruit 1988; van der Kruit & Freeman 2011).

The thick disc mass is 30% the total baryonic mass (i.e. of both the thin and thick disc combined, where the baryonic mass is $M_\star = 1 \times 10^{11} M_\odot$). The number of all the disc particles is $n_{\text{bar}} = 1 \times 10^6$, each with mass $m_D = 9.2 \times 10^4 M_\odot$. The dark matter halo is modelled as a Plummer sphere

Table 1. Properties of the fiducial simulation used in this study.

Property	r_D	h_z^{thin}	h_z^{thick}	$n_{\text{disc}}^{\text{thin}}$	$n_{\text{disc}}^{\text{thick}}$	m_d	r_H	n_{halo}	m_h	ϵ
Value	4.7 kpc	0.3 kpc	0.9 kpc	700 000	300 000	$9.2 \times 10^4 M_\odot$	10 kpc	500 000	$3.2 \times 10^5 M_\odot$	150 pc

Notes. From left to right the columns correspond to the characteristic radius of both the thin and thick disc, the characteristic height of the thin disc, the characteristic height of the thick disc, the number of particles in the thin disc, the number of particles in the thick disc, the mass of the disc particles, the characteristic radius of the dark matter halo, the number of particles in the dark matter halo, the mass of the halo particles and the softening length.

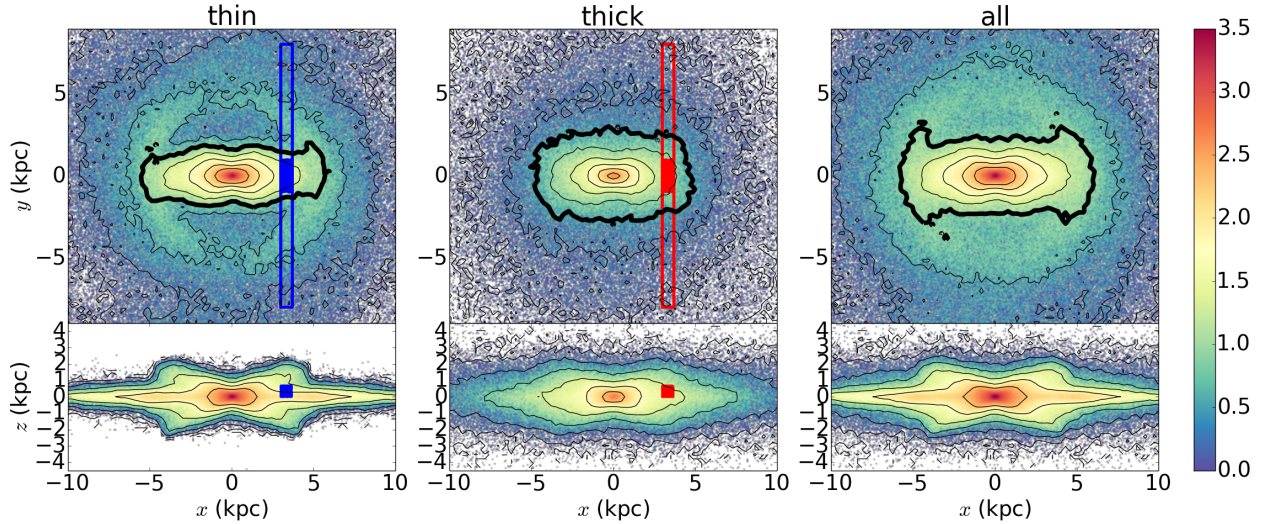


Fig. 2. Surface density maps for the thin and thick disc stars (*first and second columns*, respectively) and all the stars in the disc (*third column*). The *top panels* show the *xy* (face-on) projection and the *bottom panels* show the *xz* (edge-on) projection of surface density. The blue and red shaded regions indicate the selected particles at the end of the bar discussed in Sect. 5 and in Figs. 14 and 15 (see text).

(Binney & Tremaine 2008) with mass $M_H = 1.6 \times 10^{11} M_\odot$, characteristic radius $r_H = 10$ kpc, and $n_{\text{halo}} = 5 \times 10^5$ particles, each with mass $3.2 \times 10^5 M_\odot$. In Table 1 we summarise some of the main properties of the simulations used in this study.

To run the simulations we employ the Tree-SPH code of Semelin & Combes (2002), in which gravitational forces are calculated using a hierarchical tree method (Barnes & Hut 1986); for a full description of the code the reader is referred to Semelin & Combes (2002). As there is no gas in these simulations the SPH part of the code is not employed and the gravitational forces are calculated using a tolerance parameter $\theta = 0.7$ and include terms up to the quadrupole order in the multipole expansion. A Plummer potential is used to soften gravity at scales smaller than $\epsilon = 150$ pc. The equations of motion are integrated using a leapfrog algorithm with a fixed time step of $\Delta t = 0.25$ Myr.

In the snapshots taken from the end of the simulation, after 9 Gyr of evolution, once a bar and a b/p form – which are those used for most of the analyses in the rest of this paper – we renormalise the bar length to be 5 kpc, similar to values found for the Milky Way and external galaxies (Gadotti 2011; Wegg et al. 2015). We measure the bar length using two methods: by eye, where the bar length is taken as the distance between the centre of the galaxy to the outer tip of the bar component, usually where the spiral arms begin (e.g. Martin 1995), and by using the ellipse fitting method, where the bar length is measured as the semi-major axis of maximum ellipticity in the bar (e.g. Erwin 2005). The difference between these two measurements is of the order of 20%, as found in previous studies (e.g. Martin 1995; Erwin 2005) and we adopt the average value of the two methods.

3. Morphology of thin and thick disc bars and b/p’s

We explore some of the morphological properties of bars and b/p bulges which form in set-ups with both a thin and thick disc. A full description of the morphological properties of bars and b/p bulges in thin+thick disc set-ups with different thick disc masses and scalelengths will be discussed in Fragkoudi et al. (in prep.); here we outline the most important aspects for this study.

In our simulations we can separate by construction which stars originate in the thin disc component and which stars originate in the thick disc component, and we track them as the system evolves self-consistently. In what follows we refer to the bar (or b/p) as seen exclusively in the thin disc population as the “thin disc bar” (or thin disc b/p) and that seen exclusively in the thick disc population as the “thick disc bar” (or thick disc b/p).

In Fig. 2 we show the surface density of the thin (left) and thick disc (middle), and the total surface density for all the particles in the disc (right panel) at the end of the simulation after 9 Gyr once the bar and b/p have formed. We draw thick contour lines¹ around isophotes of the bar in the left and middle panels to draw the eye to some interesting features, namely that the thick disc bar is rounder than in the thin disc component. From ellipse fitting of the isodensity contours, we find that the thin disc bar has an axial ratio about half that of the thick disc at the end of the bar. This is not surprising, since previous studies have shown that bars forming in hotter components are weaker (e.g. Combes et al. 1990; Athanassoula 2003). However, it is interesting to note that even though the thin

¹ The thick contours are not for the same isophote level in the thin and thick disc.

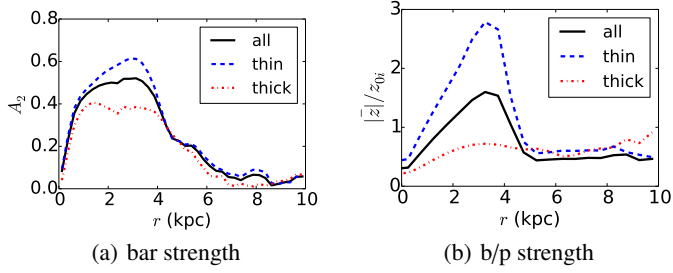


Fig. 3. *a)* Bar strength A_2 as a function of radius at the end of the simulation for the thin (dashed blue line) and thick (dash-dotted red line) discs separately and the total bar strength (solid black line). The thick disc bar is weaker than the thin disc bar. *b)* Strength of the thin and thick disc b/p (see Eq. (5)) and the total b/p bulge strength (colours as in plot *a*).

and thick discs are evolving concurrently in the same gravitational potential, the morphology of the thin and thick disc bar is different (see Bekki & Tsujimoto 2011a,b; Di Matteo 2016; Athanassoula et al. 2016, 2017; Debattista et al. 2017; see also Wozniak & Michel-Dansac 2009, on how a kinematically cold population produced from a gaseous component is mapped into a b/p bulge). We show in Sect. 5 that this is due to the kinematically hotter component which exchanges less angular momentum with the dark matter halo, and due to the large radial excursions of the thick disc particles which carry high angular momentum particles to the inner regions of the galaxy. We also see that the morphology of the b/p is different in the two populations. The thin disc b/p has a much more prominent X-shape than the thick disc b/p, which looks more “boxy” (see also Bekki & Tsujimoto 2011a,b; Di Matteo 2016; Debattista et al. 2017; Athanassoula et al. 2017). This again is due to the orbital structure of the two populations and to the fact that the colder population is more efficiently trapped in the resonances.

The different shapes of the bar and b/p in the thin and thick disc can also be seen more quantitatively by examining Fig. 3, where we show the bar strength (left) and the b/p strength (right) for the thin and thick disc component, and for the total population. The bar strength is obtained using the now standard Fourier decomposition method (see e.g. Athanassoula et al. 2013). We obtain the Fourier components by azimuthally decomposing the mass distribution as

$$a_m(R) = \sum_{i=0}^{n_i} m_i \cos(m\theta_i), m = 0, 1, 2, \dots, \quad (2)$$

$$b_m(R) = \sum_{i=0}^{n_i} m_i \sin(m\theta_i), m = 0, 1, 2, \dots, \quad (3)$$

where R is the radius, n_i is the number of particles in an annulus around the radius, m_i is the mass of the particle, and θ_i is the azimuthal angle. We perform this decomposition for the thin and thick discs separately, and for all the particles of the disc together.

A single value for bar strength is then obtained for each snapshot as

$$A = \max(A_{2j}) = \max \left(\frac{\sqrt{a_{2j}^2(R) + b_{2j}^2(R)}}{a_{0j}(R)} \right), \quad (4)$$

where j stands for either the thin, thick, or total mass distribution.

The b/p strength is derived by taking the median of the absolute value of the distribution of particles in the vertical (z) direction, in a given radial bin of a snapshot seen edge-on, and with the bar viewed side-on (similarly to Martínez-Valpuesta & Athanassoula 2008). To obtain the b/p strength we renormalise the median $|\tilde{z}|$ to the characteristic scale-height of the disc population at the start of the simulation, z_{0i} , before the b/p formation and subsequent vertical heating. Then for each snapshot the maximum of these values over radius is taken as the boxy/peanut strength, i.e.

$$C = \max \left(\frac{|\tilde{z}|}{z_{0i}} \right). \quad (5)$$

In this way, the thin and thick disc will have the same b/p strength at the start of the simulation (which ensures that although the thick disc has a greater scaleheight at the beginning of the simulation, it will not have a stronger b/p).

In Fig. 3, we see that the strength of the thick disc bar is $\sim 50\%$ smaller than that of its thin disc counterpart, while the thick disc b/p strength is 20% that of the thin disc b/p. This is due to the higher velocity dispersion in the thick disc, which leads to the stars being less tightly bound in the bar-b/p instability. On the other hand, the thin disc bar appears stronger because the particles in the thin disc are colder, and are thus on more circular orbits to begin with and can therefore be more easily trapped in the bar instability. We also see that the total bar and b/p strength, as well as the morphology of the bar and b/p of the total disc, are a combination of the two separate thin and thick disc components, i.e. they are between the two extremes, as seen in the third panel of Fig. 2 and the solid black lines in Fig. 3. The degree to which the morphology will look like one or the other component will depend on how much mass is in each component and on the relative scalelength of the two discs.

It is important to note that, because the b/p is weaker in the thick disc component, the signature of the b/p will appear at greater heights above the plane for the thick disc stars than for the thin disc stars. By “signature” of the b/p, we refer to the dip in the density distribution of stars along the bar major axis (as is seen for example in the magnitude distribution of red giant clump stars in the Milky Way; e.g. Nataf et al. 2010; McWilliam & Zoccali 2010; Ness et al. 2012; Rojas-Arriagada et al. 2014). This can be seen in Fig. 4, where we take cuts in z along the length of the bar (which is placed along the x -axis, as in Fig. 2) and plot histograms of the number of particles in the thin and thick disc. Very close to the plane, the signature of the b/p is not visible in either of the two components, and instead there is one central peak in the density distribution of stars (see Fig. 4a). At slightly greater heights above the plane (Fig. 4b) the signature of the peanut begins to show up in the thin disc, while it is not seen in the thick disc. However, as we go to greater heights above the plane (Fig. 4c) the peanut signature also appears in the thick disc, although the signature is weaker than in the thin disc. Additionally, the separation between the peaks of the peanut increases for greater heights above the plane (see also Ness et al. 2012; Wegg & Gerhard 2013; Gonzalez et al. 2015; Di Matteo 2016; Gómez et al. 2016; Debattista et al. 2017), as occurs also for the two peaks in the magnitude distribution of red clump stars along longitude $l = 0$ in the Milky Way (see e.g. Rojas-Arriagada et al. 2014). Therefore, in order to be able to see the (weak) dip in the thick disc stars in these models, it is necessary to go to greater heights above the plane.

In Fig. 5 we show the projection in xz of the fraction of the thin disc surface density compared to the total. This shows in

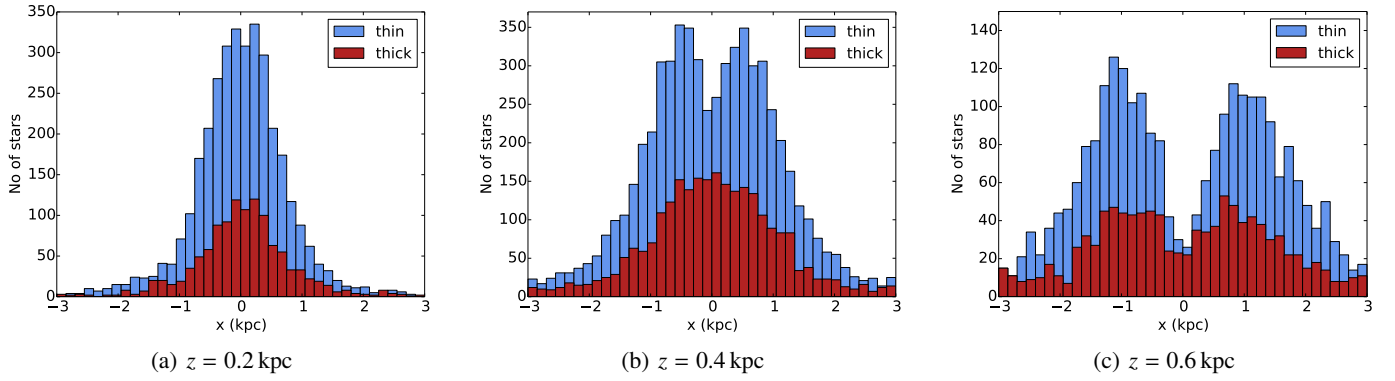


Fig. 4. Distribution of stars along the bar major axis at different heights above the plane, starting from close to the plane on the *left* and moving further away from the plane towards the *right*. The signature of the b/p bulge is weaker and appears at greater heights above the plane for the kinematically hotter component.

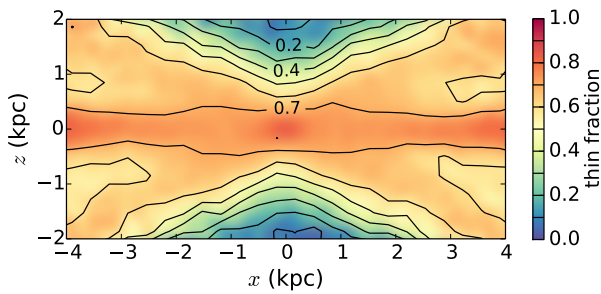


Fig. 5. Fraction of thin disc stars in the xz plane (the bar is placed along the x -axis) compared to the total (thin+thick disc). In models with both a thin and a thick disc, the fraction of thin disc stars decreases with distance from the plane, while the fraction of the thick disc stars correspondingly increases.

which areas of the disc above and below the plane the thin and thick disc components dominate the density distribution. The thin disc component dominates in the central regions close to the plane and is responsible for the strong X-shape of the b/p bulge. On the other hand, the thick disc fraction dominates at regions further out above the plane. Thus, we see that if we associate the thick disc with a metal-poor component, and the thin disc with a metal-rich component we would recover a vertical metallicity gradient in these models (see also Bekki & Tsujimoto 2011a,b; Di Matteo 2016; Debattista et al. 2017) as will also be shown in upcoming work using a model specifically adapted for comparison with the Milky Way.

4. Line-of-sight velocity of thin and thick discs in b/p's

In this section we explore the line-of-sight (los) velocity for this model of a disc galaxy with both a thin and a thick disc population.

In the left panel of Fig. 6 we show the los velocity of all the particles in the disc for different heights above the plane, as indicated by the colours in the top left panel (where z is given in kpc), at the start of the simulation before the bar and the b/p form. We see that the galaxy does not exhibit cylindrical rotation in the central regions. In the right panel we show Δv ,

$$\Delta v = |\langle v_{\text{los,thin}} \rangle| - |\langle v_{\text{los,thick}} \rangle|, \quad (6)$$

where v_{los} is the line-of-sight velocity of the thin and thick disc and Δv is the difference between the absolute value of the average

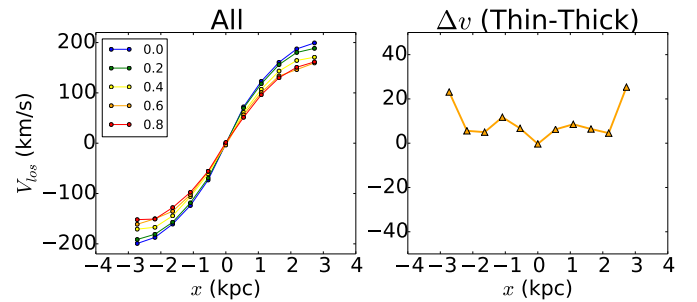


Fig. 6. *Left:* line-of-sight velocity of the disc in the central few kpc, (for all the particles) at the start of the simulation before the bar and b/p form for different heights above the plane as indicated in the top left corner (values are in kpc). *Right:* difference between the absolute value of v_{los} of the thin and thick disc components, Δv (see Eq. (6)). The thin disc has higher los velocities than the thick disc at the start of the simulation before the bar-b/p forms.

(for different heights above the plane) of these two line-of-sight velocities. By examining the right panel of Fig. 6 we see that, as expected, at the start of the simulation, the thin disc has a higher los velocity than the thick disc.

In Fig. 7 we show a 2D map of the los velocity for all the particles (top), for the thin disc particles (middle), and for the thick disc particles (bottom) of the final snapshot of the fiducial simulation after the bar and b/p are formed. The orientation of the bar is along the x -axis, i.e. side-on, and the white contours show the outline of the surface density of the corresponding component. As is typical of models containing bars and b/p bulges, there is overall cylindrical rotation in the model with the los velocity being independent of height above the plane (see Iannuzzi & Athanassoula 2015, for a complete study of the 2D kinematics of the b/p bulge in models with a single disc). We also see that the thin and thick disc components exhibit cylindrical rotation until about $z \sim 1$ kpc above the plane of the galaxy.

We further explore the los velocity after the bar-b/p formation of each disc component separately in Fig. 8. We show the los velocity in the b/p bulge for different heights below the plane of the galaxy. We separate the particles into those originating in the thin and thick disc components (first and second columns, respectively), and also plot the los velocity of all the particles together (third column). In the fourth column we show the difference in los velocities, Δv (as given by Eq. (6)), between the thin and thick disc. From top to bottom we show three different

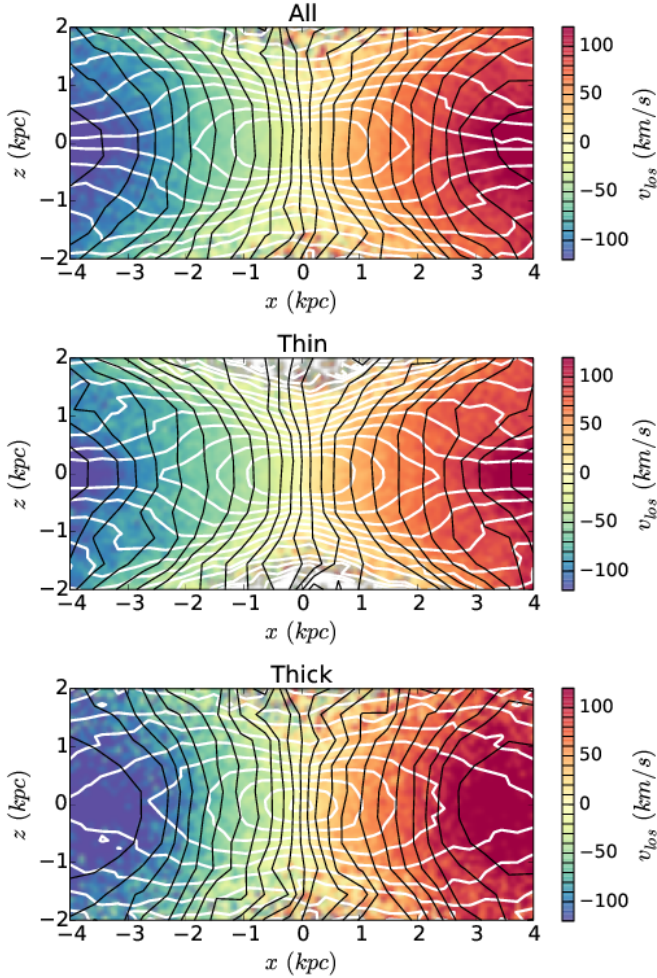


Fig. 7. Two-dimensional velocity field of all the stars (*top*), of the thin disc stars (*middle*), and of the thick disc stars (*bottom*) in the fiducial simulation after 9 Gyr of evolution after the bar and b/p have formed. The white contours show the surface density of each component, while the black isovelocity contours are plotted at intervals of 10 km s^{-1} .

orientations of the bar: the side-on orientation where the bar is along the x -axis, an orientation where the bar is at 30 degrees to the line of sight (similar to the view we have of the Milky Way), and end-on, i.e. where the bar is along the y -axis. The surface density in xz of the stellar particles in each of these orientations is shown in the fifth column.

We see again that, apart from the cylindrical rotation in all the stars combined (third column of Fig. 8), the thin and thick discs (first and second column of Fig. 8) also exhibit cylindrical rotation separately, as seen in the 2D map of v_{los} in Fig. 7. Additionally, we see that the v_{los} depends on the orientation of the bar with respect to the line of sight. For end-on orientations, the v_{los} has a steeper gradient than the side-on orientations. Interestingly, we see that the v_{los} is not the same in the thin and thick disc components: we see that the thick disc stars have a *higher* v_{los} than thin disc stars in the outer regions of the b/p bulge, which is quantified by Δv in the fourth column. This is contrary to what occurs at larger radii, i.e. outside the b/p bulge region, as can be seen in Fig. 9 where we show a zoom-out of the v_{los} of the thin and thick disc; the shaded box shows the area being examined in Fig. 8. The higher v_{los} in the b/p region for thick disc stars is also contrary to what is seen at the start of the simulation before the bar forms (see right panel,

Fig. 6) where the thin disc has a higher v_{los} . While the higher v_{los} in the thick disc is most prominent for the side-on orientation of the bar (up to $\sim 40 \text{ km s}^{-1}$), it can also be seen when the bar has an orientation of 30 degrees with respect to the line of sight towards the galactic centre ($\sim 20\text{--}30 \text{ km s}^{-1}$, i.e. similar to what is seen for the Milky Way), and in the end-on orientation ($\sim 10 \text{ km s}^{-1}$).

We also show the difference between the thin and thick disc v_{los} , Δv_{los} , in 2D in Fig. 10 for the three different orientations mentioned above (from top to bottom: side-on, 30 degrees, and end-on), where again the difference in v_{los} between the two populations appears mostly at the edges of the b/p bulge. At the centre of the b/p, the thin disc can actually have a slightly higher v_{los} , especially for the end-on case. We also show Δv between the thin and thick disc in Fig. 11 for a snapshot in which the b/p is not completely symmetric yet (i.e. it is still going through the buckling phase). When the b/p is not completely symmetric there can be regions in the inner b/p where the thin disc has higher v_{los} than the thick disc, while on the opposite side of the $z = 0$ axis the thick disc will have a higher v_{los} .

Thus, in general in the outer parts of the b/p, the hot population will tend to have a higher v_{los} , while in the inner regions of the b/p this trend can be reversed, depending also on the orientation of the bar with respect to the line of sight and on the symmetry of the b/p.

This is, in fact, a characteristic signature of a kinematically hot disc component: while a dispersion dominated population, such as a classical bulge, can acquire some rotation, it cannot rotate faster than the surrounding disc component (see e.g. [Fux 1997](#); [Saha et al. 2012, 2016](#); [Saha & Gerhard 2013](#); [Di Matteo et al. 2014](#)).

5. Mapping thin and thick discs in b/p's

In this section we explore why thick disc stars have a higher v_{los} in the b/p bulge region and how this is related to the orbits, morphology, angular momenta, and birth radii of stars found in the bar-b/p region. We then relate these factors to the velocity dispersion of the thin and thick disc components.

5.1. Angular momentum exchange

The kinematics of the thin and thick disc stars in the bar-b/p bulge region can be understood in terms of the amount of angular momentum that the stars of the thin and thick disc lose via the bar instability. As has been extensively studied in the literature (e.g. [Athanassoula 2003](#); [Ceverino & Klypin 2007](#)), the disc transfers angular momentum to the halo mainly via the corotation, inner, and outer Lindblad resonances which are induced by the bar potential. In Fig. 12 we plot the angular momenta (normalised to the total angular momentum L_{tot} of the system) of the various components in the simulation as a function of time. The thin disc, which is kinematically colder than the thick disc, transfers angular momentum to the halo, which subsequently increases its angular momentum. The thick disc's angular momentum, on the other hand, slightly increases during the first 1.5 Gyr of evolution (by about 1%), after which it also proceeds to lose angular momentum via the bar instability which is transferred to the dark matter halo, although at a much slower rate than the thin disc. This initial increase in the angular momentum of the thick disc could be due to a transfer of angular momentum from the thin disc. Overall, the dark matter halo's angular momentum increases by about 16% L_{tot} , while the thin and thick discs' angular momenta decrease by about 14% and 2% L_{tot} , respectively.

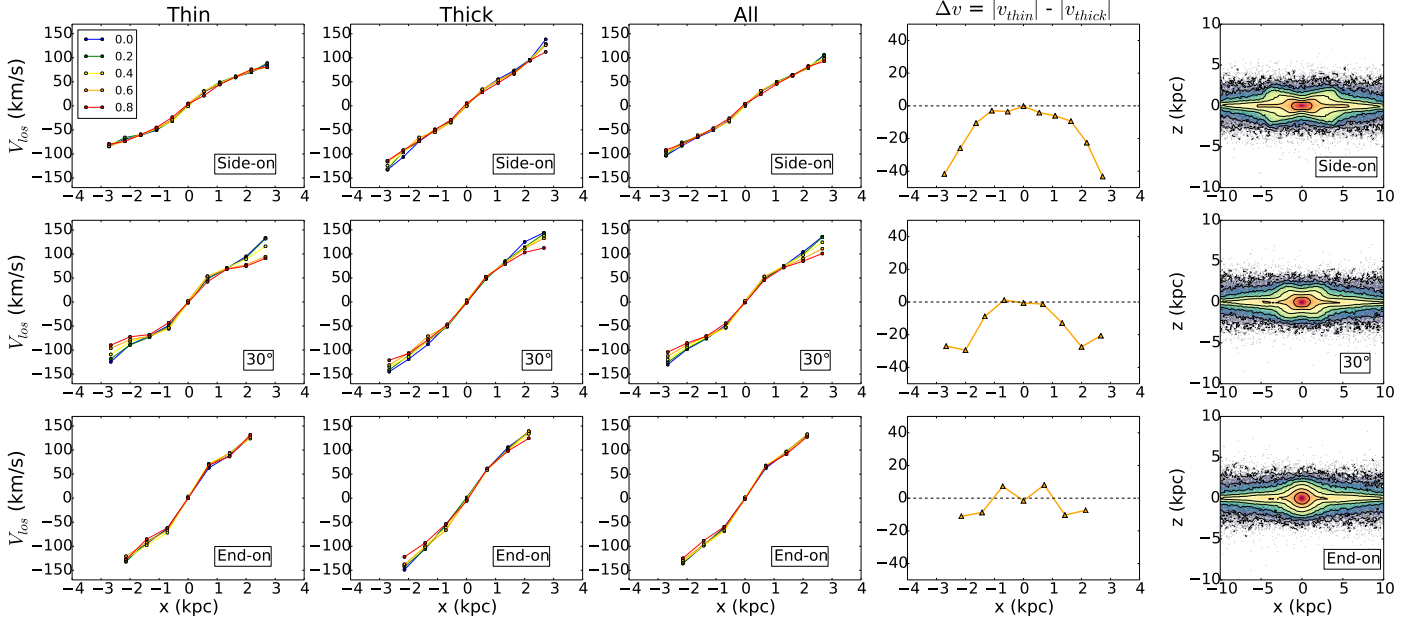


Fig. 8. Line-of-sight velocity for “slits” at different heights above the plane, as indicated in the *top left inset*, for three orientations of the bar, side-on (bar semi-major axis at 90 degrees to the los, *top row*), 30 degrees to the line of sight (similar to the Milky Way orientation, *middle row*) and end-on (bar at 0 degrees to the los, *bottom row*). The *first column* shows the los velocity of the thin disc stars, the *second column* the thick disc stars, and the *third column* gives the los velocity for all the stars. The *fourth column* shows the average difference Δv between the thin and thick disc los velocities (see Eq. (6)). The *fifth column* shows the surface density of the simulation for the given orientation. For side-on and Milky Way-like orientations the thick disc has higher los velocities than the thin disc.

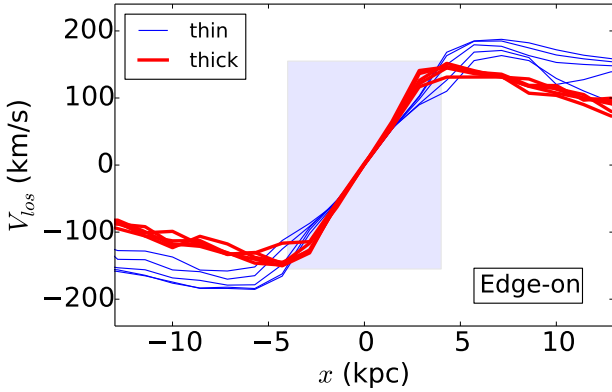


Fig. 9. Line-of-sight velocity of the thin (blue) and thick (red) disc stars at the end of the simulation after the bar and b/p form. The shaded region indicates the zoomed-in region shown in Fig. 8 and the lines correspond to different heights above the plane, as in Fig. 8.

The decrease in angular momentum is thus more significant for thin disc stars than for thick disc stars. The amount of angular momentum which is transferred from the discs to the dark matter halo is related to the radial velocity dispersions of the discs. Stars from a colder population with a lower radial velocity dispersion will get trapped more easily by the bar instability and thus the transport of angular momentum from the disc to the halo will be more efficient.

The fact that the higher v_{los} of thick disc stars is most evident for side-on orientations of the bar suggests that the bar orbits are responsible for this behaviour. Indeed, as we can see from the morphology of the thin and thick disc bar in Fig. 2, focusing on the thick isodensity contours, the thick disc bar is rounder than the thin disc bar. This can also be understood in terms of the models’ orbital structure, as can be seen in Fig. 13, where we plot

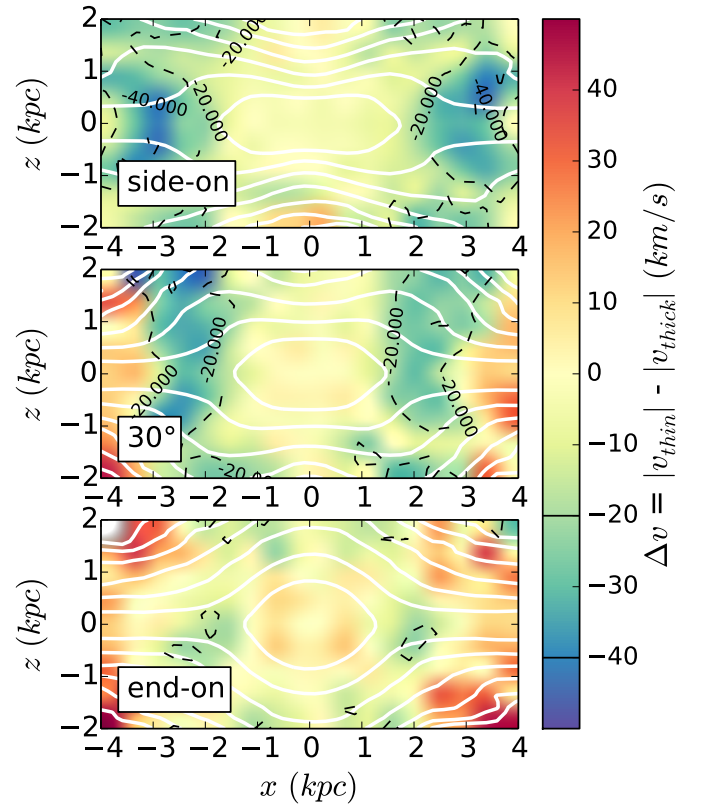


Fig. 10. Difference Δv_{los} between the line-of-sight velocity of the thin and thick disc in 2D for the three orientations shown in Fig. 8. Isodensity contours are shown in white.

typical orbits found in the bar region, which originate from the thin and thick disc. These orbits are taken by selecting the stars in the shaded region of Fig. 2 and tracing the orbits over a short

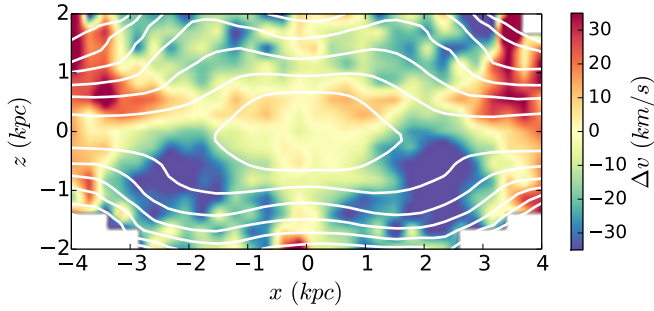


Fig. 11. Difference Δv_{los} between the line-of-sight velocity of the thin and thick disc in 2D for a snapshot where the b/p in the model is not completely symmetric, as indicated by the white isodensity contours.

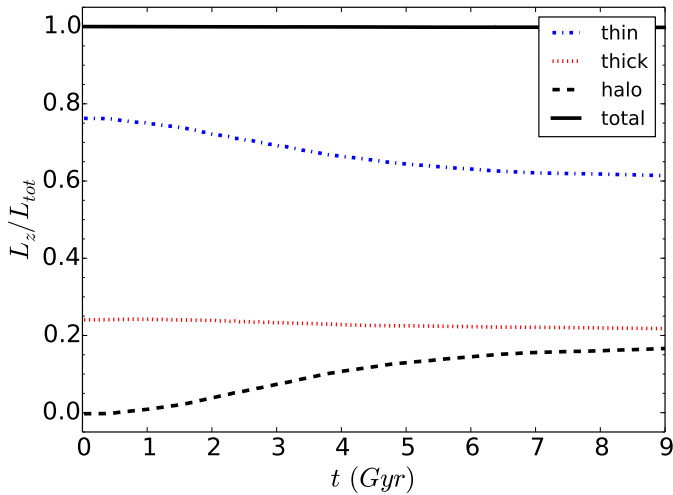


Fig. 12. Total angular momentum of the thin (dash-dotted blue) and thick (dotted red) discs, of the dark matter halo (dashed black), and of the total angular momentum in all the components (solid black) as a function of time, normalised by the total angular momentum. The discs lose angular momentum, which is transferred to the dark matter halo, while the thin disc loses a much higher percentage than the thick disc (see text).

period of time while maintaining the bar along the x -axis. We then examined these orbits by eye and found a common trend, i.e. that thick disc bar orbits in general tend to be rounder than thin disc orbits with the same semi-major axis, like the example shown in Fig. 13. We will show a full orbital analysis of thin and thick disc stars in bar and b/p bulges in upcoming work.

To further explore this, we examine the specific angular momentum of stars in the outer parts of the b/p bulge (the selected stars are indicated by the shaded and unshaded coloured regions in Fig. 2). We show, in Fig. 14, the angular momenta of stars selected from this region at the start of the simulation when the disc is axisymmetric (top row) and at the end of the simulation once the bar and b/p form (bottom row). In the left column we plot the angular momenta of all the stars along the line of sight (i.e. we include the foreground and background disc contamination) in the region of $x = 3.2\text{--}3.5$ kpc and $z = 0.2\text{--}0.5$ kpc (indicated by the unshaded boxed region in Fig. 2), while in the right column we only select stars in the bar region (as indicated by the shaded regions in Fig. 2).

We see some interesting features in the angular momentum distribution. As expected, at the start of the simulation the thin disc stars have higher angular momenta than the thick disc stars

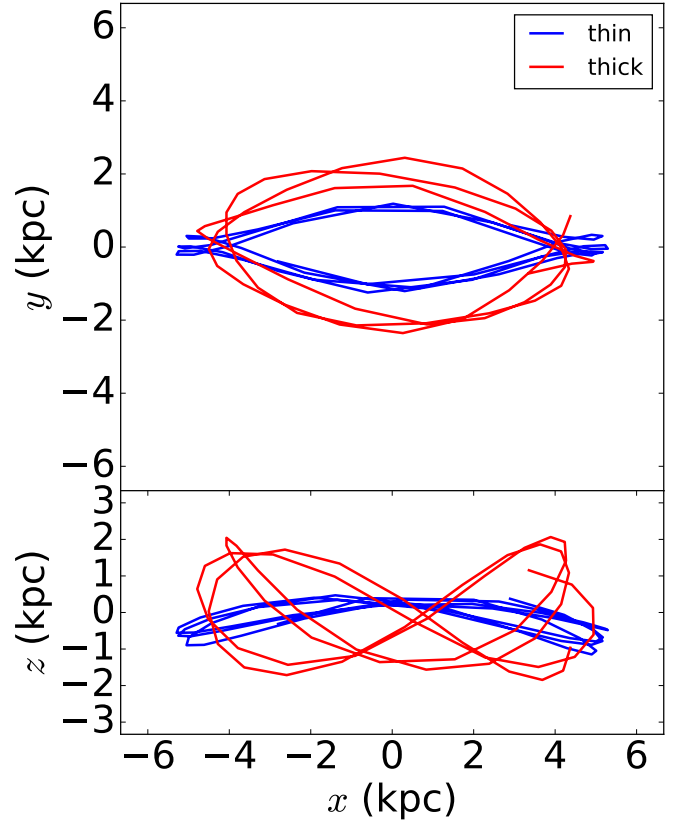


Fig. 13. Typical thin (blue) and thick (red) disc orbits in the bar region (see text for details). The orbits look like the well-known x_1 orbits in the face-on projection (the bar is rotated to be along the x -axis). For similar radii, thick disc orbits tend to be rounder than thin disc orbits.

(Fig. 14 top left plot). Also at the start of the simulation, at a radius that will eventually be the end of the bar-b/p region, the thin disc stars also have higher angular momenta than the thick disc stars, with a clear peak of the angular momentum of the thin disc stars at higher values of L_z (top right plot). At the end of the simulation, once the bar and b/p have formed, we see a bimodality in the angular momenta of the thin disc stars in the bottom left panel of Fig. 14: there is a peak at low angular momenta (around $250 \text{ km s}^{-1} \text{ kpc}$) and a peak at high angular momenta (around $1000 \text{ km s}^{-1} \text{ kpc}$), while the angular momenta of the thick disc stars have spread out and the peak is shifted to slightly higher angular momenta compared to the start of the simulation. The low angular momentum peak of stars in the thin disc occurs because the thin disc loses a significant amount of angular momentum from the inner regions, and ends up with stars on elongated bar orbits. The peak at higher angular momenta for the thin disc stars is due to the stars in the disc on largely circular orbits, outside the bar. This is confirmed by examining the angular momenta of thin disc stars in the bar region (bottom right plot), where we see that once we exclude the disc from the selection we maintain only the low angular momentum stars in the bar. We also see (in the bottom right plot of Fig. 14) that in the bar region, the thick disc stars have a tail of high angular momenta. These stars have higher angular momenta partly because thick disc stars do not lose as much angular momentum via the bar instability as thin disc stars do (see Fig. 12) and partly because, as we discuss below, thick disc stars from large radii are trapped in the bar instability.

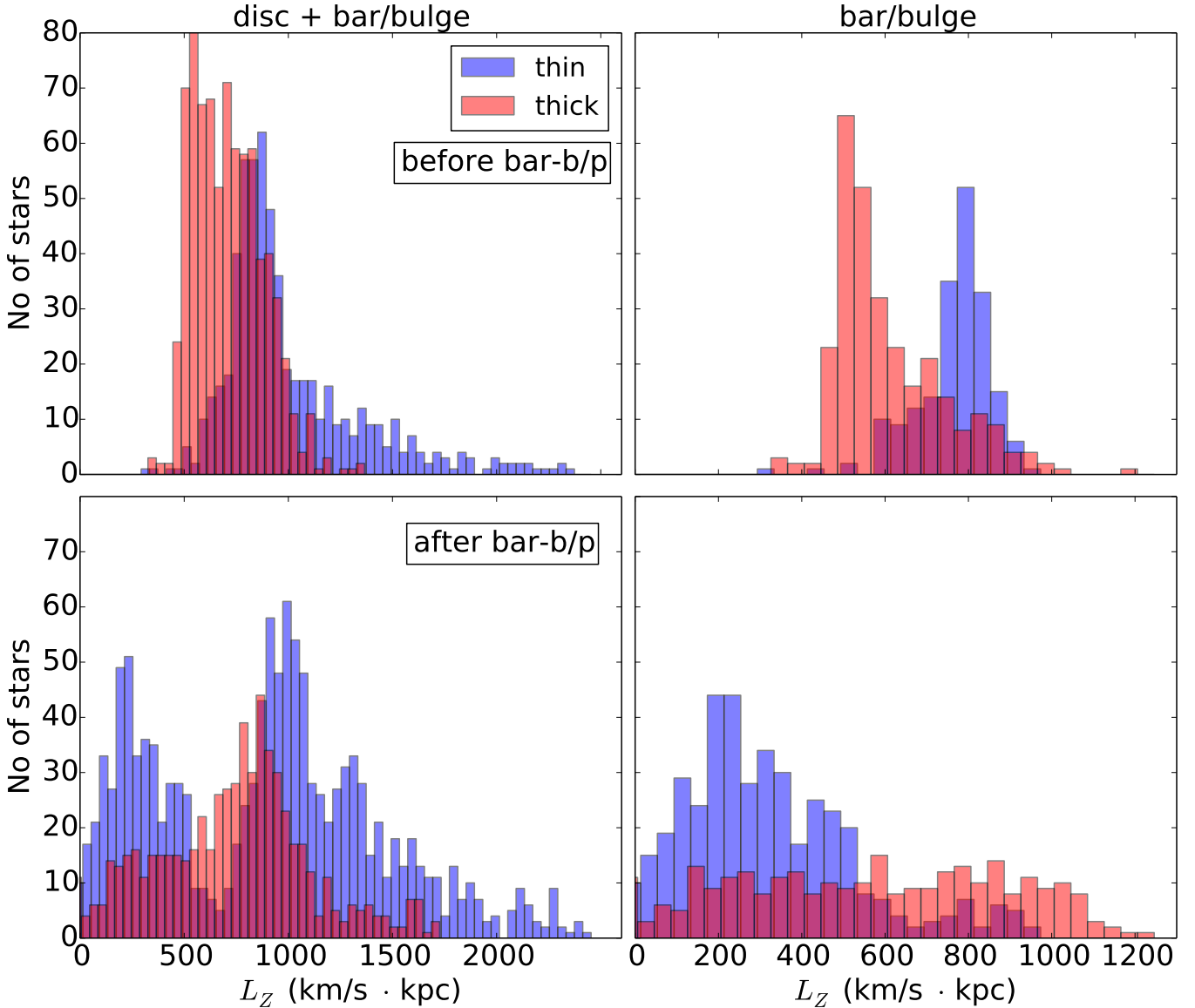


Fig. 14. Angular momentum distribution of the thin (blue) and thick (red) disc particles. *Left:* particles are chosen from a region including the disc and bar, i.e. $x = 3.2\text{--}3.5$ kpc, $z = 0.2\text{--}0.5$ kpc, and $y = -8\text{--}8$ kpc (unshaded region of Fig. 2). In these plots the foreground and background disc contamination are explicitly included. *Right:* angular momentum distribution of the thin (blue) and thick (red) disc particles in the bar-b/p region, i.e. $x = 3.2\text{--}3.5$ kpc, $z = 0.2\text{--}0.5$ kpc, and $y = -1\text{--}1$ kpc (shaded region in Fig. 2). The *top row* shows the angular momenta for the first snapshot when the disc is axisymmetric, i.e. before the bar and b/p bulge form, while the *bottom row* shows the angular momenta after bar and b/p formation. Focusing on the particles in the bar/bulge region after the bar and b/p form (*bottom right panel*), we note that the thick disc particles have a tail of higher angular momentum than the thin disc stars.

5.2. Birth radii

In addition to the fact that thin disc stars lose more angular momentum than thick disc stars, we find that the tail of high angular momentum stars in the thick disc is also due to stars which originate further out in the disc, but due to their large radial excursions can be found in the inner regions of galaxies, in the bar-b/p region.

To explore this, in Fig. 15 we plot the birth radii (i.e. the positions of the particles at the start of the simulation) of the selected particles from the shaded regions in Fig. 2. The solid and dashed black lines indicate the average radius of the particles and the outer Lindblad resonance (OLR) at the end of the simulation. The colour and size of the points in the plot are a function of the angular momentum at the end of the simulation, i.e. after

the bar-b/p formation. It is clear that particles maintain a memory of their original angular momentum since stars which are born at larger radii also tend to have the largest angular momentum at the end of the simulation (see also [Martinez-Valpuesta & Gerhard 2013](#); [Di Matteo et al. 2014](#)). We see in Fig. 15a that the thin disc particles originate from a region around the average radius, with some migration from both inside and outside this radius. When examining the birth radii of thick disc particles in Fig. 15b which end up in the b/p region, we see that there are a number of stars whose birth radii are much larger than those of the thin disc. This is due to the fact that thick disc stars have larger radial excursions and can therefore end up in the inner parts of the disc. Therefore, these stars have high angular momenta at the end of the simulation. These large radial excursions are due to the higher radial velocity dispersion in the outer parts of the thick disc.

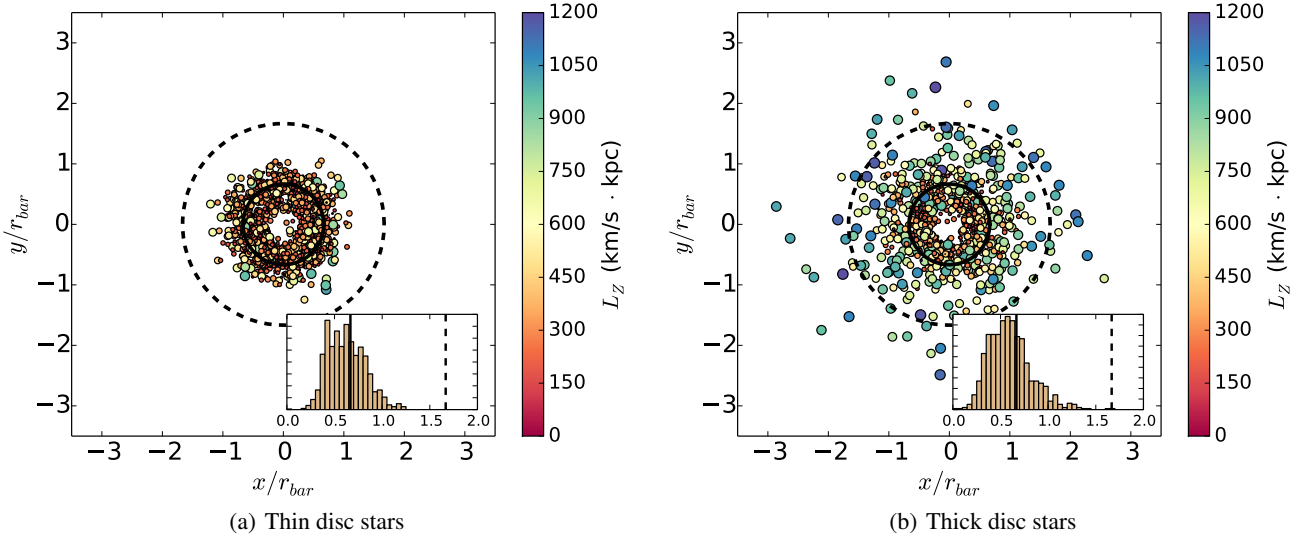


Fig. 15. Instantaneous position of particles selected near the edge of the bar (shaded regions in Fig. 2) at the start of the simulation for the thin (left) and thick (right) disc. The x - and y -axis are normalised to the bar length r_{bar} . The solid black circle gives the average radius of these stars at the end of the simulation and the dashed black circle delineates the OLR. The inset shows a histogram of the guiding radii of these stars at the start of the simulation. The guiding radii of the thin disc stars are quite similar to the instantaneous radius of the particles, while the guiding radii of the thick disc stars are limited to a smaller range than the instantaneous positions because these stars have larger radial excursions. The size and colour of the points indicate the angular momentum of these particles at the end of the simulation. The stars born at larger radii are also the ones that have larger angular momenta at the end of the simulation.

This migration is mostly due to blurring, rather than churning, caused by stars in the thick disc that are on elongated orbits; this is consistent with the fact that we expect churning to be less efficient for hot populations (Vera-Ciro et al. 2014). This is corroborated by examining the insets of Fig. 15, where we show the guiding radius of the particles at the start of the simulation, which are calculated as in Minchev et al. (2014), where the guiding radius is given by

$$r_g = \frac{L}{v_c}, \quad (7)$$

where $L = rv_\phi$ is the angular momentum of the particle and v_c is the circular velocity at the corresponding radius.

We see that the guiding radii of the thick disc particles are in general smaller than the instantaneous birth radii and that all these stars have guiding radii inside the OLR (see also Halle et al. 2015), while stars can have instantaneous birth radii outside the OLR. Therefore, we see that thick disc stars enter the bar-b/p region due to blurring, i.e. because the particles are on elongated orbits.

5.3. Dependence on thick disc velocity dispersion

The radial velocity dispersion profiles of discs at the time of bar and b/p formation influence two factors which will determine their los velocity in the bar-b/p region: the angular momentum transfer from the discs to the halo through the bar instability and the radii from which stars can reach the bar-b/p region. By increasing the radial velocity dispersion in the thick disc there is less angular momentum transfer from the disc to the halo, and stars can reach the bar-b/p region from larger radii; these factors will lead to higher los velocities of thick disc stars compared to the thin disc stars in the bar-b/p regions.

In terms of what we expect the radial velocity dispersion profile of the thick disc to be, there is little observational evidence, at

both low and high redshifts, when bars and boxy/peanut bulges first formed. There have been some recent studies from the CALIFA survey which show that the velocity dispersion for late-type galaxies seems to increase in their outer parts (see Fig. 10 in Falc3n-Barroso et al. 2017). However, this velocity dispersion is the los dispersion and does not correspond only to the radial velocity dispersion, σ_r . Furthermore, it corresponds to the velocity dispersion at low redshifts – not the velocity dispersion at the time that bars and b/p bulges might have formed in these galaxies. From the theoretical side, cosmological zoom-in simulations, such as the one studied in Bird et al. (2013), show that the oldest stellar populations, which are also the hottest, can have quite high radial velocity dispersions in the outer parts, show a dip in velocity dispersion at intermediate radii, and then have rising values again towards the centre (see their Fig. 4). Therefore, the shape of the thick disc radial velocity dispersion profile produced in our fiducial initial conditions seems to be relatively common, at least in simulated galaxies.

Nonetheless, since we do not know what the radial velocity dispersion profile of galaxies will be at redshifts $z \sim 1-2$ – when bars are expected to start forming in discs (e.g. Sheth et al. 2008; Simmons et al. 2014; Gadotti et al. 2015) – we explore the effect of changing this profile on the los velocity of thin and thick disc stars in the b/p bulge. We can thus determine what trends we can expect if the radial velocity dispersion of the thin and thick disc were different to begin with (see also Debattista et al. 2017, for a discussion on the effects of σ_r on the morphology of the b/p bulge). To this end, we carried out a number of test simulations where we imposed various radial velocity dispersion profiles for the thick disc (see Fig. A.1).

We find that whether or not the thick disc stars have a higher los velocity compared to the thin disc stars will depend (at least in part) on the shape of the initial velocity dispersion profile (i.e. before bar formation). Specifically, it depends on the difference in velocity dispersion between the thin and the thick disc in the regions from which particles eventually get trapped in the bar

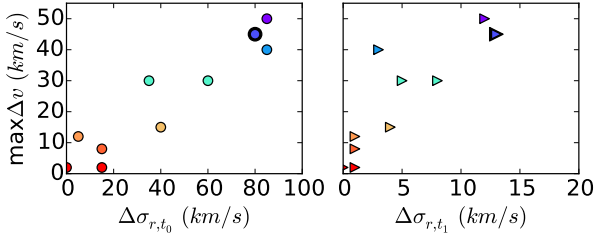


Fig. 16. *Left:* dependence of the difference in los velocity between thin and thick disc stars in the b/p as a function of the difference in radial velocity dispersion at $r = r_{b/p}$ at the start of the simulation. The colour-coding is as a function of the y -axis and is added to help guide the eye in Fig. A.1. The model analysed in this paper is indicated by a black outline. *Right:* same as left panel, but for the final snapshot of the simulation.

and b/p bulge. If the radial velocity dispersion of the thin and thick disc are similar, then the morphology of the bar will also be similar in the two discs, and we would not expect to see a higher los velocity in the thick disc stars. Indeed, there needs to be quite a large difference between the initial radial velocity dispersions of these discs in order to observe the difference in v_{los} , as can be seen in the left panel of Fig. 16 where we plot the maximum difference between the average los velocity of the thin and thick disc, Δv , as a function of the difference between the velocity dispersion in the thin and thick discs $\Delta\sigma$ at the start of the simulation (at a radius corresponding to the edge of the b/p at the end of the simulations) for a number of test simulations. We see that there is a general trend where the larger the difference between the radial velocity dispersions in the thin and thick disc at the start of the simulation, the larger the difference in the los velocities once the bar and b/p forms. We also plot the difference in velocity dispersion of the thin and thick disc at the radius where we measure Δv at the end of the simulation, for reference, and we show this in the right panel of Fig. 16. We see that the trend remains, but that the difference in velocity dispersion between the cold and hot population is reduced.

This of course indicates that the properties of the bar and b/p in thin and thick discs will be highly dependent on the properties of the discs at the time of bar formation/disc settling. Thus, if thick discs are formed with higher velocity dispersions than thin discs, which is what observations (Wisnioski et al. 2015) and simulations (Bird et al. 2013; Grand et al. 2016) of galaxies at higher redshifts point to, the morphology and kinematics of the thick disc bar will be considerably different to that of the thin disc bar. We suggest, very tentatively, that it could be possible to use the relation found in Fig. 16 to place constraints on the difference between the velocity dispersions of the thin and thick disc at the time the bar was formed.

6. Comparison with observations

In this section we compare the findings of this study to some of the available observations of the morphology and kinematics of the Milky Way bulge, even though the model presented in this paper is not fitted to represent the Milky Way. Do we see these trends, i.e. a higher (or equal) los velocity in kinematically hotter components than in the kinematically colder ones in the b/p bulge of the Milky Way? How does the morphology of the b/p bulge change with height above the plane and for different stellar populations?

6.1. Morphology

Using data from the ARGOS survey (Freeman et al. 2013), which explored the metallicity and kinematics of stars in the inner 3.5 kpc of the Milky Way bulge, Ness et al. separate the stars in their sample into different components according to their metallicity (Ness et al. 2013a,b). They label the main components they find in the Milky Way bulge as A, B, and C, where A is the most metal-rich component with $[Fe/H] > 0$, component B with $0 > [Fe/H] > -0.5$, and component C, $-0.5 > [Fe/H] > -1$. They also find a small fraction of stars in the bulge with lower metallicities, labelled components D and E, with $[Fe/H] < -1$, which make up just a small percent of the stars in the bulge.

The fraction of each component changes with height above the plane, which leads to a vertical metallicity gradient (Ness et al. 2013a); close to the plane the metal-rich component A has a larger contribution to the total density, while further away from the plane, at $b = -10$ degrees, its contribution decreases and that of the metal-poor component C increases. Component B seems to be more or less the same at all heights above the plane. Although in our models we only have two components – a thin and thick disc which could be thought of as a metal-rich and metal-poor component, respectively – we see that having a metal-poor thick disc and a metal-rich thin disc would give qualitatively similar results, i.e. a higher fraction of the metal-rich component close to the plane and a higher fraction of the metal-poor component further out from the plane (see Fig. 5).

In the *Gaia*-ESO Survey (GES; Gilmore et al. 2012), the stars in the bulge are separated into two components, metal-poor and metal-rich, where the metal-poor component is also kinematically hotter than the metal-rich component (Rojas-Arriagada et al. 2014). It can be seen in Fig. 10 of Rojas-Arriagada et al. (2014) that for the field closest to the plane (p1m4 at $b = -4$), there is no dip in the magnitude distribution of the red clump giants in their sample. However, for fields further away from the plane (e.g. at p0m6, $b = -6$) there is a clear dip in the magnitude distribution of the red clump stars of the metal-rich component; however, it is not visible in the metal-poor component. For field m1m10, which is at $b = -10$, and therefore the furthest away from the plane, the dip in the metal-rich component becomes wider, while there seems to be a hint of a dip in the metal-poor component as well (which in Rojas-Arriagada et al. 2014, is interpreted as being due to a volume effect). This dip at higher latitudes for the metal-poor component is very similar to what we see in our Fig. 4, where we take cuts parallel to the z plane and explore the density along the los for the thin and thick disc component. That is, we find that the signature of the b/p bulge in the kinematically hotter (thick) disc component appears weaker and further away from the plane than for the kinematically cold (thin) disc population. In Rojas-Arriagada et al. (2014) there is also a faint dip in the field p7m9, which is at 7 degrees of longitude and which is likely not due to the b/p bulge. We note that while the bimodality at p7m9 may be spurious, we suspect that the bimodality at m1m10 is not since this signature is seen both in GES and in ARGOS. In the ARGOS data (Fig. 20 in Ness et al. 2013a) we see a bimodality in population B at $l = 0$, $b = -10$. Since the metal-poor population of GES includes part of what would correspond to population B of ARGOS, and since the ARGOS $l = 0$, $b = -10$ field is very close to the GES m1m10 field, it is not unreasonable to suggest that the bimodality in the metal-poor population in m1m10 in GES is not spurious. However, as the model used

in this work is not specifically adapted to fit the MW bulge, we do not explore this further and we refer to future work where we will use a precise model for the MW to explore in detail the signature of the b/p bulge in terms of l , b .

6.2. Kinematics

In the ARGOS survey, component A is the kinematically coldest component, and the components become hotter for B and C while maintaining cylindrical rotation (Ness et al. 2013b). Components D and E, on the other hand, do not have cylindrical rotation. This seems to point to the fact that populations A, B, and C likely have a disc-like origin. We also see that component B, which is kinematically hotter than component A, has a higher l_{os} velocity than component A in the outer regions of the bulge, as we find in this study, which indicates that component B is likely due to a kinematically hotter disc. This is similar to the interpretation given by Ness et al. (2013b) for component B (although not due to the l_{os} velocity), who find that the chemical properties of population B are similar to those of the “early thin disc” and which in Di Matteo et al. (2014) and Di Matteo (2016) was interpreted as the “young thick disc”. Regarding component C from Ness et al. (2013b), although it has a higher velocity dispersion, it does not appear to have a higher l_{os} velocity. This could be due to another origin for component C, i.e. other than a thick disc, while it could also be due to some contamination from halo stars which do not have a disc-like origin (see e.g. Debattista et al. 2017) and therefore do not have much rotation to begin with.

We also see similar behaviour in the GES data (Rojas-Arriagada et al. 2014), where, as mentioned above, the metal-rich and metal-poor components are also kinematically cold and hot, respectively. We see a hint (although within the errors) of a higher l_{os} velocity in their metal-poor population as compared to the metal-rich population in the bulge (see their Fig. 11). This behaviour is to be expected, should this population be due to the thick disc population which can participate in the bar instability.

On the other hand, kinematic data for the bulge region from the APOGEE survey Ness et al. (2016, where the data is separated as in the ARGOS survey, into components A, B, C, etc.) does not seem to recover the same behaviour in terms of the l_{os} velocity as in the aforementioned surveys, with component B and C from APOGEE both rotating more slowly than component A. It remains to be understood why this discrepancy exists between the different surveys and whether this is just an issue of low number statistics in some fields.

7. Summary and conclusions

We examine the morphology and kinematics of the bar-b/p bulge region in N -body simulations of isolated disc galaxies with both a (kinematically cold) thin disc and a (kinematically hot) thick disc, which evolve secularly over 9 Gyr. By construction, we can separate the particles in our models into those originating from the thin and thick disc, and can therefore trace how the two discs are mapped into the bar-b/p. Owing to the different kinematic properties of these two discs at the time the bar and b/p form, their stars have different morphological and kinematic properties when mapped into the bar and b/p.

In terms of morphology, we find the following:

- The bar that forms from stars from the kinematically cold thin disc is stronger ($\sim 50\%$) and has an axial ratio which is almost half that of the thick disc bar (see Figs. 2 and 3).
- The b/p bulge forming out of the thin disc is stronger and has a more pronounced X-shape than the thick disc b/p bulge (see Figs. 2 and 3).
- The signature of the b/p, i.e. the dip in the density distribution along the bar major axis, is weaker for thick disc stars and appears at greater heights above the plane compared to the thin disc stars (see Fig. 4).
- The distance between the peaks of the b/p increases for greater heights above the plane (see Fig. 4).

In terms of kinematics, we see the following:

- The model has cylindrical rotation, in the total stellar population (i.e. thin + thick disc stars) and also in each component separately (see Figs. 7 and 8).
- Contrary to what is seen in the disc region outside the b/p (Fig. 9), the thick disc stars have higher l_{os} velocities than those of the thin disc in the outer regions of the b/p when the bar is viewed side-on or with an orientation similar to that in the Milky Way (40% and 20% higher v_{los} , respectively; see Fig. 8). This feature is a characteristic signature of a kinematically hot disc participating in the bar-b/p instability.
- This feature is due to the orbital structure of the thin and thick disc bars, and to the fact that stars from the thin disc get trapped on more elongated orbits in the bar region (see Fig. 13).
- The difference in orbital structure of the thin and thick disc bars is due to the angular momentum transfer from the discs to the halo. A considerable amount of angular momentum is transferred from the thin disc to the halo, while the thick disc does not lose as much angular momentum as the thin disc because it is a kinematically hotter population (see Fig. 12).
- Additionally, thick disc stars originating in the outer parts of the disc with high angular momentum, can be found in the bar region as a result of large radial excursions, i.e. due to blurring (see Figs. 14 and 15).
- We find a correlation between the difference in the initial radial velocity dispersion of the discs ($\Delta\sigma_r$) and the difference in the l_{os} velocity of the two discs in the b/p bulge region at the end of the simulation (Δv_{los} ; see Fig. 16).

The aforementioned point to the fact that the morphological and kinematic properties of bars and b/p bulges depend on the kinematic properties of their different stellar populations and therefore also on their formation mechanisms.

Acknowledgements. This work has been supported by the ANR (Agence Nationale de la Recherche) through the MOD4Gaia project (ANR-15-CE31-0007, P.I.: P. Di Matteo). F.F. is supported by a postdoctoral grant from the Centre National d’Études Spatiales (CNES). This work was granted access to the HPC resources of CINES under the allocation 2016-040507 made by GENCI.

References

- Abadi, M. G., Navarro, J. F., Steinmetz, M., & Eke, V. R. 2003, *ApJ*, 597, 21
 Aguerri, J. A. L., Méndez-Abreu, J., & Corsini, E. M. 2009, *A&A*, 495, 491
 Athanassoula, E. 1983, *IAU Symp.*, 100, 243A
 Athanassoula, E. 2003, *MNRAS*, 341, 1179
 Athanassoula, E. 2016, *Galactic Bulges*, 418, 391
 Athanassoula, E., & Sellwood, J. A. 1986, *MNRAS*, 221, 213
 Athanassoula, E., Machado, R. E. G., & Rodionov, S. A. 2013, *MNRAS*, 429, 1949
 Athanassoula, E., Rodionov, S. A., Peschken, N., & Lambert, J. C. 2016, *ApJ*, 821, 90

- Athanassoula, E., Rodionov, S. A., & Prantzos, N. 2017, *MNRAS*, **467**, L46
- Barazza, F. D., Jogee, S., & Marinova, I. 2008, *ApJ*, **675**, 1194
- Barnes, J., & Hut, P. 1986, *Nature*, **324**, 446
- Bekki, K., & Tsujimoto, T. 2011a, *MNRAS*, **416**, L60
- Bekki, K., & Tsujimoto, T. 2011b, *ApJ*, **738**, 4
- Bensby, T., Alves-Brito, A., Oey, M. S., Yong, D., & Meléndez, J. 2011, *ApJ*, **735**, L46
- Binney, J. 1981, *MNRAS*, **196**, 455
- Binney, J., & Tremaine, S. 2008, *Galactic Dynamics*, 2nd edn. (Princeton University Press), 920
- Bird, J. C., Kazantzidis, S., Weinberg, D. H., et al. 2013, *ApJ*, **773**, 43
- Bovy, J., Rix, H.-W., Liu, C., et al. 2012, *ApJ*, **753**, 148
- Brook, C. B., Kawata, D., Gibson, B. K., & Freeman, K. C. 2004, *ApJ*, **612**, 894
- Burstein, D. 1979, *ApJ*, **234**, 829
- Ceverino, D., & Klypin, A. 2007, *MNRAS*, **379**, 1155
- Combes, F., Debbasch, F., Friedli, D., & Pfenniger, D. 1990, *A&A*, **233**, 82
- Comerón, S., Elmegreen, B. G., Knapen, J. H., et al. 2011, *ApJ*, **741**, 28
- Debattista, V. P., Ness, M., Gonzalez, O. A., et al. 2017, *MNRAS*, **469**, 1587
- Di Matteo, P. 2016, *PASA*, **33**, e027
- Di Matteo, P., Haywood, M., Gómez, A., et al. 2014, *A&A*, **567**, A122
- Dwek, E., Arendt, R. G., Hauser, M. G., et al. 1995, *ApJ*, **445**, 716
- Erwin, P. 2005, *MNRAS*, **364**, 283
- Eskridge, P. B., Frogel, J. A., Pogge, R. W., et al. 2000, *AJ*, **119**, 536
- Falcón-Barroso, J., Lyubenova, M., van de Ven, G., et al. 2017, *A&A*, **597**, A48
- Fragkoudi, F., Athanassoula, E., Bosma, A., & Iannuzzi, F. 2015, *MNRAS*, **450**, 229
- Fragkoudi, F., Athanassoula, E., & Bosma, A. 2016, *MNRAS*, **462**, L41
- Freeman, K., Ness, M., Wylie-de-Boer, E., et al. 2013, *MNRAS*, **428**, 3660
- Fux, R. 1997, *A&A*, **327**, 983
- Gadotti, D. A. 2009, *MNRAS*, **393**, 1531
- Gadotti, D. A. 2011, *MNRAS*, **415**, 3308
- Gadotti, D. A., Seidel, M. K., Sánchez-Blázquez, P., et al. 2015, *A&A*, **584**, A90
- Gilmore, G., Randich, S., Asplund, M., et al. 2012, *The Messenger*, **147**, 25
- Gómez, A., Di Matteo, P., Stefanovitch, N., et al. 2016, *A&A*, **589**, A122
- Gonzalez, O. A., Zoccali, M., Debattista, V. P., et al. 2015, *A&A*, **583**, L5
- Grand, R. J. J., Springel, V., Gómez, F. A., et al. 2016, *MNRAS*, **459**, 199
- Halle, A., Di Matteo, P., Haywood, M., & Combes, F. 2015, *A&A*, **578**, A58
- Haywood, M., Di Matteo, P., Lehnert, M. D., Katz, D., & Gómez, A. 2013, *A&A*, **560**, A109
- Haywood, M., Di Matteo, P., Snaith, O., & Lehnert, M. D. 2015, *A&A*, **579**, A5
- Hohl, F. 1971, *ApJ*, **168**, 343
- Howard, C. D., Rich, R. M., Clarkson, W., et al. 2009, *ApJ*, **702**, L153
- Iannuzzi, F., & Athanassoula, E. 2015, *MNRAS*, **450**, 2514
- Kunder, A., Koch, A., Rich, R. M., et al. 2012, *AJ*, **143**, 57
- Kunder, A., Rich, R. M., Koch, A., et al. 2016, *ApJ*, **821**, L25
- Lütticke, R., Dettmar, R.-J., & Pohlen, M. 2000, *A&AS*, **145**, 405
- Martig, M., Minchev, I., & Flynn, C. 2014, *MNRAS*, **442**, 2474
- Martin, P. 1995, *AJ*, **109**, 2428
- Martínez-Valpuesta, I., & Athanassoula, E. 2008, in *Pathways Through an Eclectic Universe*, eds. J. H. Knapen, T. J. Mahoney, & A. Vazdekis, *ASP Conf. Ser.*, **390**, 463
- Martínez-Valpuesta, I., & Gerhard, O. 2013, *ApJ*, **766**, L3
- Martínez-Valpuesta, I., Shlosman, I., & Heller, C. 2006, *ApJ*, **637**, 214
- McWilliam, A., & Zoccali, M. 2010, *ApJ*, **724**, 1491
- Menéndez-Delmestre, K., Sheth, K., Schinnerer, E., Jarrett, T. H., & Scoville, N. Z. 2007, *ApJ*, **657**, 790
- Minchev, I., Chiappini, C., & Martig, M. 2014, *A&A*, **572**, A92
- Minchev, I., Martig, M., Streich, D., et al. 2015, *ApJ*, **804**, L9
- Nataf, D. M., Udalski, A., Gould, A., Fouqué, P., & Stanek, K. Z. 2010, *ApJ*, **721**, L28
- Ness, M., & Lang, D. 2016, *AJ*, **152**, 14
- Ness, M., Freeman, K., Athanassoula, E., et al. 2012, *ApJ*, **756**, 22
- Ness, M., Freeman, K., Athanassoula, E., et al. 2013a, *MNRAS*, **430**, 836
- Ness, M., Freeman, K., Athanassoula, E., et al. 2013b, *MNRAS*, **432**, 2092
- Ness, M., Zasowski, G., Johnson, J. A., et al. 2016, *ApJ*, **819**, 2
- Pfenniger, D., & Friedli, D. 1991, *A&A*, **252**, 75
- Portail, M., Wegg, C., & Gerhard, O. 2015, *MNRAS*, **450**, L66
- Qu, Y., Di Matteo, P., Lehnert, M. D., & van Driel, W. 2011, *A&A*, **530**, A10
- Quinn, P. J., Hernquist, L., & Fullagar, D. P. 1993, *ApJ*, **403**, 74
- Rodionov, S. A., Athanassoula, E., & Sotnikova, N. Y. 2009, *MNRAS*, **392**, 904
- Rojas-Arriagada, A., Recio-Blanco, A., Hill, V., et al. 2014, *A&A*, **569**, A103
- Saha, K., & Gerhard, O. 2013, *MNRAS*, **430**, 2039
- Saha, K., Martínez-Valpuesta, I., & Gerhard, O. 2012, *MNRAS*, **421**, 333
- Saha, K., Gerhard, O., & Martínez-Valpuesta, I. 2016, *A&A*, **588**, A42
- Schönrich, R., & Binney, J. 2009, *MNRAS*, **399**, 1145
- Semelin, B., & Combes, F. 2002, *A&A*, **388**, 826
- Shen, J., Rich, R. M., Kormendy, J., et al. 2010, *ApJ*, **720**, L72
- Sheth, K., Elmegreen, D. M., Elmegreen, B. G., et al. 2008, *ApJ*, **675**, 1141
- Simmons, B. D., Melvin, T., Lintott, C., et al. 2014, *MNRAS*, **445**, 3466
- Skokos, C., Patsis, P. A., & Athanassoula, E. 2002, *MNRAS*, **333**, 847
- Snaith, O., Haywood, M., Di Matteo, P., et al. 2015, *A&A*, **578**, A87
- Stinson, G. S., Bovy, J., Rix, H.-W., et al. 2013, *MNRAS*, **436**, 625
- Tsikoudi, V. 1979, *ApJ*, **234**, 842
- van der Kruit, P. C. 1988, *A&A*, **192**, 117
- van der Kruit, P. C., & Freeman, K. C. 2011, *ARA&A*, **49**, 301
- Vera-Ciro, C., D'Onghia, E., Navarro, J., & Abadi, M. 2014, *ApJ*, **794**, 173
- Wegg, C., & Gerhard, O. 2013, *MNRAS*, **435**, 1874
- Wegg, C., Gerhard, O., & Portail, M. 2015, *MNRAS*, **450**, 4050
- Weiland, J. L., Arendt, R. G., Berriman, G. B., et al. 1994, *ApJ*, **425**, L81
- Wisnioski, E., Förster Schreiber, N. M., Wuyts, S., et al. 2015, *ApJ*, **799**, 209
- Wozniak, H., & Michel-Dansac, L. 2009, *A&A*, **494**, 11
- Yoachim, P., & Dalcanton, J. J. 2006, *AJ*, **131**, 226

Appendix A: Radial velocity dispersions of test simulations

For the analysis discussed in Sect. 5.3 we used a number of test simulations with a variety of shapes for the radial velocity dispersion profile of the thick disc in order to examine how the results discussed in the paper depend on this profile. We show in Fig. A.1 the radial velocity dispersion profiles of the test models

used to construct Fig. 16, where the colour-coding used in Fig. A.1 corresponds to that in Fig. 16. The vertical black line indicates the end of the b/p bulge radius, which is where the maximum difference between the los velocities of the thin and thick disc ($\max\Delta_v$) can be seen in Fig. 8. This is where the difference between the radial velocity dispersion of the thin and thick disc were taken for Fig. 16.

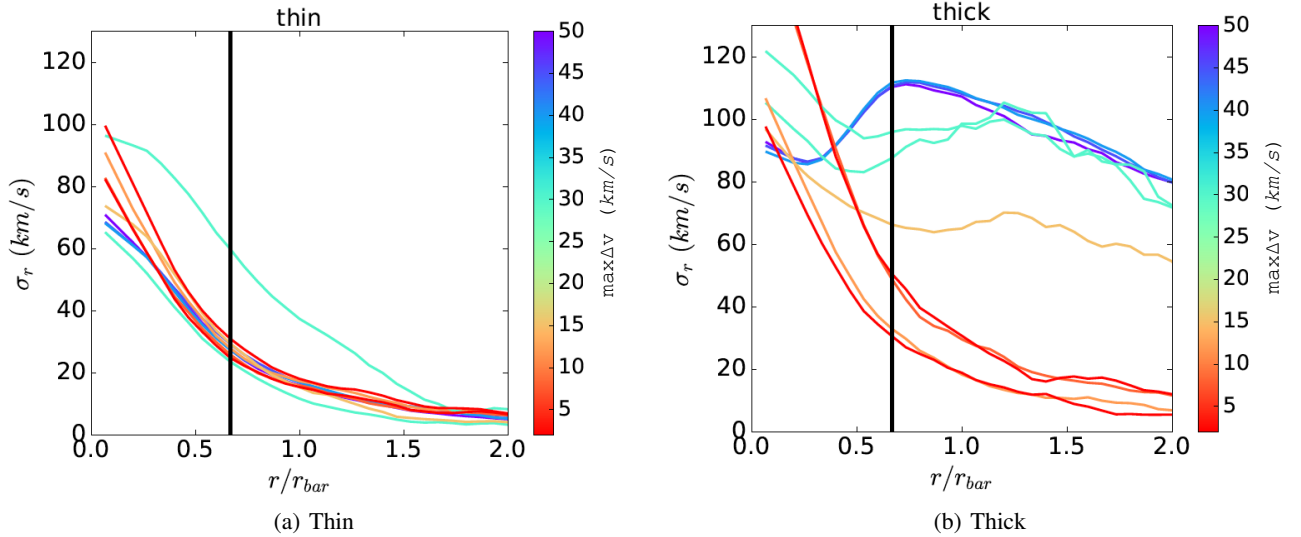


Fig. A.1. Initial radial velocity dispersion σ_r of the thin (*left*) and thick disc (*right*) for a number of test simulations, which were used to construct Fig. 16. The colour-coding corresponds to the colour bar in Fig. 16, i.e. according to the maximum Δv of the model. The vertical black line indicates the end of the b/p bulge.